

Modelling mid-Z element atmospheres for strongly-magnetized neutron stars

Kaya Mori^{1,2}*, Wynn C.G. Ho^{3,4}†

¹Department of Astronomy and Astrophysics, University of Toronto, 50 St. George Street, Toronto, Ontario, M5S 3H4, Canada

²Canadian Institute for Theoretical Astrophysics, University of Toronto, 60 St. George Street, Toronto, Ontario, M5S 3H8, Canada

³Harvard-Smithsonian Center for Astrophysics, 60 Garden Street, Cambridge, MA, 02138, USA

⁴Kavli Institute for Astrophysics and Space Research, Massachusetts Institute of Technology, Cambridge, MA, 02139, USA

28 August 2018

ABSTRACT

We construct models for strongly-magnetized neutron star atmospheres composed of mid-Z elements (carbon, oxygen and neon) with magnetic fields $B = 10^{12}$ – 10^{13} G and effective temperatures $T_{\text{eff}} = (1 - 5) \times 10^6$ K; this is done by first addressing the physics relevant to strongly-magnetized plasmas and calculating the equation of state and polarization-dependent opacities. We then obtain the atmosphere structure and spectrum by solving the radiative transfer equations in hydrostatic and radiative equilibrium. In contrast to hydrogen opacities at the relevant temperatures, mid-Z element opacities are dominated by numerous bound-bound and bound-free transitions. Consequently, temperature profiles are closer to grey profiles, and photosphere densities are lower than in the hydrogen case. Mid-Z element atmosphere spectra are significantly softer than hydrogen atmosphere spectra and show numerous absorption lines and edges. The atmosphere spectra depend strongly on surface composition and magnetic field but weakly on surface gravity. Absorption lines are primarily broadened by motional Stark effects and the (unknown) surface magnetic field distribution. When magnetic field variation is not severe, substructure in broad absorption features can be resolved by (phase-resolved) CCD spectroscopy from *Chandra* and *XMM-Newton*. Given the multiple absorption features seen in several isolated neutron stars, it is possible to determine the surface composition, magnetic field, temperature, and gravitational redshift with existing X-ray data; we present qualitative comparisons between our model spectra and the neutron stars 1E1207.4–5209 and RX J1605.3+3249. Future high-resolution X-ray missions such as *Constellation-X* will measure the gravitational redshift with high accuracy by resolving narrow absorption features; when combined with radius measurements, it will be possible to uniquely determine the mass and radius of isolated neutron stars.

Key words: atomic processes – magnetic fields – stars: atmospheres – stars: neutron

1 INTRODUCTION

Recent observations by *Chandra* and *XMM-Newton* detected spectral features from isolated neutron stars (INSs). A single or multiple absorption features have been found from nearby radio-quiet NSs (Haberl et al. 2003; van Kerkwijk et al. 2004; Haberl et al. 2004b; Zane et al. 2005; Schweppe et al. 2005; Haberl 2006) and two broad absorption features were detected from 1E1207.4–5209 (hereafter 1E1207; Sanwal et al. 2002; Mereghetti et al. 2002; Mori et al. 2005). In fact, 1E1207 is unique among these INSs since one of the features appears above 1 keV, while the other INSs have absorption features at $E \simeq 0.2$ – 0.7 keV. Identification of the observed spectral

features will not only allow a measurement of the surface composition and magnetic field strength B but also constrain the nuclear equation of state via a measurement of the gravitational redshift z_g , where z_g is given by $(1 + z_g) = (1 - 2GM/Rc^2)^{-1/2}$ and M and R are the NS mass and radius, respectively.

The surface composition is usually assumed to be hydrogen because the fast sedimentation time (due to the strong surface gravity) causes the lightest elements to rise to the top (Alcock & Illarionov 1980) and only a tiny amount of hydrogen is required to produce an optically thick atmosphere (Romani 1987). Hydrogen atmospheres in strong magnetic fields have been studied in great detail by addressing the complicated properties of strongly-magnetized dense plasmas (Pavlov et al. 1995; Lai & Salpeter 1997; Potekhin et al. 1999; Potekhin & Chabrier 2003, 2004). Partially-ionized hydrogen atmosphere models show spectral fea-

* e-mail: kaya@cita.utoronto.ca

† e-mail: wynnho@slac.stanford.edu

tures, such as the proton cyclotron line, photo-ionization edge, and atomic transition lines at $E \lesssim 1$ keV (Ho et al. 2003; Potekhin et al. 2004). However, hydrogen atmospheres cannot produce strong spectral features at $E \gtrsim 1$ keV because (1) the binding energy of a hydrogen atom never exceeds ~ 1 keV at any B (Lai 2001; Sanwal et al. 2002), (2) QED effects significantly reduce line strengths at $B \gtrsim 7 \times 10^{13}$ G (Ho & Lai 2003, 2004; van Adelsberg & Lai 2006), and (3) the fraction of hydrogen molecular ions (which may have transition lines above 1 keV; Turbiner & López Vieyra 2004) is negligible ($< 10^{-6}$) at $B \lesssim 10^{15}$ G and $T \gtrsim 10^6$ K (Potekhin & Chabrier 2004). Therefore, spectral features at $\gtrsim 1$ keV (such as the 1.4 keV absorption line of 1E1207) hint at a non-hydrogenic element atmosphere on the NS surface (Sanwal et al. 2002; Hailey & Mori 2002; Mori & Hailey 2006). Also, recent theoretical studies suggest that a hydrogen layer on the surface may be rapidly depleted by diffuse nuclear burning or pulsar winds, thus exposing the heavier elements that lie underneath (Chang et al. 2004; Chang & Bildsten 2004).

The few existing non-hydrogenic atmosphere models (Miller 1992; Rajagopal et al. 1997) are far from complete, due mainly to a lack of accurate atomic data for multi-electron ions in the high magnetic field regime and crude treatment of ionic motional and non-ideal effects. In this paper, we construct mid-Z element (carbon, oxygen and neon) atmosphere models that are compatible with the high quality X-ray data of *Chandra* and *XMM-Newton*. We only consider magnetic field strengths $B = 10^{12} - 10^{13}$ G and effective temperatures $T_{\text{eff}} = (1 - 5) \times 10^6$ K because QED effects may become important at higher magnetic fields (Ho & Lai 2004, and references therein) and molecules may become abundant at lower temperatures (Medin & Lai 2006a). QED effects on mid-Z element atmosphere structure and spectra will be studied in future work (Ho & Mori 2007). We also defer investigation of strongly-magnetized helium atmospheres due to non-trivial motional Stark effects and possible contamination by helium molecules (Mori & Heyl 2007).

We briefly describe here several major improvements of our mid-Z element atmosphere models over the previous atmosphere models by Miller (1992) (for helium and mid-Z elements) and Rajagopal et al. (1997) (for iron).

(1) The previous non-hydrogenic atmosphere models assume that bound electrons are in the ground Landau state (adiabatic approximation). However, the adiabatic approximation is not valid for the low B and high atomic number Z regime that we consider in this paper. For instance, the ionization energy of the innermost electron of $Z = 6-10$ element ions at $B = 10^{12}$ G is underestimated by 5–10% in the adiabatic approximation.

(2) Numerous bound states and transitions are needed to construct mid-Z element atmospheres. The model of Miller (1992) does not include bound-bound transitions, while the iron atmosphere model of Rajagopal et al. (1997) utilizes rather crude atomic line data (the energy values and oscillator strengths have as much as 10% and a factor of 2 uncertainties, respectively). We explicitly calculated line energies and oscillator strengths for numerous transitions. For instance, nearly 600 transition lines are included in the oxygen atmosphere model at $B = 10^{12}$ G.

(3) In the case of hydrogen and helium, it is non-trivial to take into account the effects of a finite nuclear mass (Potekhin 1994; Bezchastnov et al. 1998). However, a simple perturbative approach, introduced by Pavlov & Meszaros (1993), is applicable to mid-Z element atmospheres due to the larger nuclear mass and binding energies.

(4) All the previous magnetized atmosphere models, except

the recent hydrogen atmosphere models of Potekhin et al. (2004), adopt polarization vectors assuming the plasma is fully-ionized. However, such atmosphere models may not produce correct spectra and absorption line profiles at low temperatures when the plasma is partially-ionized (Bulik & Pavlov 1996; Potekhin et al. 2004). In our model, we explicitly compute polarization vectors by taking into account the effects of bound-bound and bound-free transitions.

(5) Our radiative transfer code has been extensively tested for partially-ionized hydrogen atmospheres at various magnetic field strengths (Ho et al. 2003; Potekhin et al. 2004). The code can be made applicable to mid-Z element atmospheres in which numerous line and edge features are present. We solve the coupled radiative transfer equations for the two photon polarization normal modes, unlike the polarization-averaged opacities used by Miller (1992).

In this paper, we present each step in the construction of mid-Z element atmosphere models. We address important physical effects in strongly-magnetized dense plasmas, following the partially-ionized hydrogen calculations of Potekhin & Chabrier (2003), Ho et al. (2003) and Potekhin et al. (2004). Sections 2, 3, and 4 discuss the atomic physics, equation of state, and opacities, respectively, that we use in the modelling; more details can be found in Mori & Hailey (2002) and Mori & Hailey (2006). Some aspects of the radiative transfer calculation are given in Section 5; details of the radiative transfer scheme are described in Ho & Lai (2001) and Ho et al. (2003). Section 6 shows our atmosphere structure results, and our model spectra are discussed in Section 7; we compare our mid-Z element atmosphere models with partially ionized hydrogen atmosphere models to illustrate the differences¹. A discussion on the determination of NS parameters is given in Section 8. We compare our model spectra to the observations of INSSs in Section 9. Section 10 summarizes our results.

2 ATOMIC PHYSICS IN STRONG MAGNETIC FIELD

In a strong magnetic field, the atomic structure is quite different from the non-magnetic case. A strong magnetic field deforms the atom into a cylindrical shape when magnetic field effects are larger than Coulomb field effects, i.e., at $\beta_Z > 1$ (Landau regime), where $\beta_Z = B/(4.7 \times 10^9 Z^2 \text{ G})$. A bound electron in the Landau regime is often denoted by two quantum numbers m and v [hereafter we use (mv) to denote a bound state], where m is the magnetic quantum number and v is the longitudinal quantum number along the field line. $v = 0$ (tightly-bound) states have a larger binding energy than $v > 0$ (loosely-bound) states. When $\beta_Z \gtrsim 1$, the ground state configuration is composed of bound electrons all in tightly-bound states, i.e. $(m0)$ states. When the axisymmetry around the magnetic field is preserved, transitions with $\Delta m = 0$ and $\Delta v = \text{odd}$ or $\Delta m = \pm 1$ and $\Delta v = \text{even}$ are allowed by dipole selection rules. The former transitions occur in the longitudinal polarization mode ($\alpha = 0$, parallel to B), while the latter transitions occur in the circular polarization modes ($\alpha = \pm 1$, transverse to B). Several forbidden transitions (e.g., $\Delta m = 2$ transition) will have non-zero oscillator strengths when the motional Stark field breaks the axisymmetry around the magnetic field (Potekhin & Chabrier 2003). However,

¹ Most of the previous NS atmosphere models have been constructed by assuming a fully-ionized plasma (Shibanov et al. 1992; Zane et al. 2000; Ho & Lai 2001; Özel 2001; Lloyd 2003). However, the atomic fraction can be sizeable for hydrogen atmospheres at the magnetic field strengths and temperatures typical of the observed INSSs (Ho et al. 2003; Potekhin et al. 2004).

we neglect these weak transitions because the motional Stark effects are significantly smaller in mid-Z element plasmas.

We developed a fast and accurate atomic code suitable for the Landau regime (Mori & Hailey 2002). The code provides atomic data to better than 1% and 10% accuracy for energies and oscillator strengths, respectively. Most importantly, by applying perturbation methods to higher Landau levels, we have an extended range of applicable magnetic fields ($\beta_Z \gtrsim 0.3$). The fast algorithm enables us to compute atomic data for numerous electron configurations within reasonable CPU time. We also evaluate bound-free cross-sections following Potekhin & Pavlov (1997).

2.1 Line broadening

Among various line broadening mechanisms in strongly-magnetized mid-Z element plasmas, motional Stark effects are the most important (Mori & Hailey 2006). As ions move randomly in a thermal plasma, coupling of the collective motion and the internal electronic structure induces a motional Stark field ($\vec{E}_{MS} = \frac{\vec{K} \times \vec{B}}{Mc}$), where \vec{K} is the pseudomomentum and M is the mass of the ion. We evaluated the energy shift caused by the motional Stark field using the perturbation method (Pavlov & Meszaros 1993; Bezchastnov et al. 1998) because the atomic mass is much heavier and the binding energies are significantly larger than in the hydrogen atom. Pavlov & Meszaros (1993) introduced a perturbation method for hydrogen atom while the method of Bezchastnov et al. (1998) is applicable to charged ions. In the perturbation method, the second-order energy shift (note that the first-order term vanishes) is given by $\frac{K_\perp^2}{2M_{\perp\kappa}}$, where K_\perp is the pseudomomentum component perpendicular to the magnetic field and $M_{\perp\kappa}$ is the transverse mass ($M_{\perp\kappa} > M$) defined in Pavlov & Meszaros (1993) and Bezchastnov et al. (1998).

For a given bound state κ , one can evaluate $M_{\perp\kappa}$ from atomic binding energies calculated under the infinite nuclear mass assumption (Pavlov & Meszaros 1993). The increase in the mass due to motional Stark effects is roughly proportional to $Z^{-2}M^{-1}$ for loosely-bound ($\nu > 0$) states. Therefore, the mass correction factor of the H-like carbon ion is smaller than that of hydrogen by a factor of ~ 400 . We computed the transverse mass for bound states with an electron in a $\nu > 0$ state using the atomic data of H-like ions since bound electrons in a $\nu > 0$ state are located at a large distance from the other bound electrons in tightly-bound states. This procedure saves a significant amount of computation time, while the results are nearly identical to those of the more rigorous calculation. Since the motional Stark field reduces the binding energy, the line profile has a wing towards lower energies (Pavlov & Meszaros 1993). In our opacity calculation, we computed a line profile for motional Stark broadening following Pavlov & Meszaros (1993) and Pavlov & Potekhin (1995).

Other less important sources of line broadening are thermal Doppler and pressure broadening. In a dense plasma, electron bound states are perturbed by electric fields from electrons (electron collisional broadening) and ions (quasi-static Stark broadening) (Salzmann 1998). We evaluated line widths by the two types of pressure broadening following Pavlov & Potekhin (1995). Pressure broadening becomes dominant only at high density ($\rho \gtrsim 10^2 \text{ g cm}^{-3}$).

2.2 Ionization balance

In local thermodynamic equilibrium (LTE) atmospheres, the ionization fraction and level population are determined by the Saha-Boltzmann equilibrium. The validity of the LTE assumption will be discussed later (see Section 6.2). We iteratively solve the generalized Saha-Boltzmann equations in a magnetic field until convergence is achieved (Khersonskii 1987; Rajagopal et al. 1997; Mori & Hailey 2006). We take into account pressure ionization by assigning occupation probabilities for bound states using the electric microfield distribution of Potekhin et al. (2002).

Figure 1 compares the effective charge (Z_{eff}) of carbon, oxygen, and neon at 10^{12} G and 10^{13} G . The effective charge is defined as $Z_{\text{eff}} = \sum_i x_i Z_i$, where Z_i and x_i are the charge and the number fraction of ions of the i -th type ($\sum_i x_i = 1$). We adopt the same temperature ($T = 3 \times 10^6 \text{ K}$) to illustrate the density dependence. In all cases, the degree of ionization decreases with density until pressure ionization becomes important at high density (e.g., $\rho \sim 10^2 \text{ g cm}^{-3}$ at $B = 10^{12} \text{ G}$). Magnetized hydrogen plasmas exhibit a similar behavior (Potekhin et al. 1999), though pressure ionization becomes important at lower densities in hydrogen atmospheres.

The ion fractions have a strong dependence on magnetic field. The degree of ionization decreases at higher magnetic fields since the binding energy increases. Note that an unmagnetized carbon plasma is highly ionized ($Z_{\text{eff}} \simeq 5-6$) even at low temperatures (Potekhin et al. 2005). At higher magnetic fields, pressure ionization takes place at higher density because the size of atoms and ions is smaller.

At high magnetic fields and low temperatures, molecules may be formed in the atmosphere (Lai 2001). We find that neutral carbon becomes abundant at $T \lesssim 10^6 \text{ K}$ and $B = 10^{13} \text{ G}$. Since we do not take into account any molecular transitions, our models become less accurate in the regime where molecular contamination is non-negligible. Medin & Lai (2006a) calculate binding energies of non-hydrogenic molecules using density-functional theory. Using their results, we solve the Saha equation for dissociation equilibrium between the C atom and C_2 molecule (Lai & Salpeter 1997). Figure 2 shows the fractional ratio of the C atom and C_2 molecule at $B = 10^{13} \text{ G}$. The solid curve is the density-temperature profile of a carbon atmosphere with $B = 10^{13} \text{ G}$ and $T_{\text{eff}} = 10^6 \text{ K}$ (see Section 6). Despite the fact that the internal degrees of freedom in molecules (such as ro-vibrational states) can enhance molecular abundance by up to two orders of magnitude (Mori & Heyl 2007), we find that molecules can be safely ignored in our study.

3 EQUATION OF STATE

Given the results from Section 2.2, we compute the equation of state (EOS) of magnetized mid-Z element atmospheres with

$$P(\rho, T) = P_{id}^e + P_{id}^i + P_{ex}^{ee} + P_{ex}^{ei} + P_{ex}^{ii}. \quad (1)$$

The first two terms (P_{id}^e and P_{id}^i) represent the ideal gas pressure of electrons and ions. Our calculation of P_{id}^e takes into account the Landau quantization and electron degeneracy in a strong magnetic field. In a dense plasma, non-ideal effects are important, and they can induce negative excess pressure from electron-electron (P_{ex}^{ee}), electron-ion (P_{ex}^{ei}) and ion-ion coupling (P_{ex}^{ii}). We compute the excess pressure following Ichimaru et al. (1987), Potekhin et al. (1999), and Potekhin & Chabrier (2003).

Figure 3 shows the normalized pressure (P/NkT , where N is the baryon number density) of a carbon plasma at different magnetic field strengths and temperatures. We also plot the different

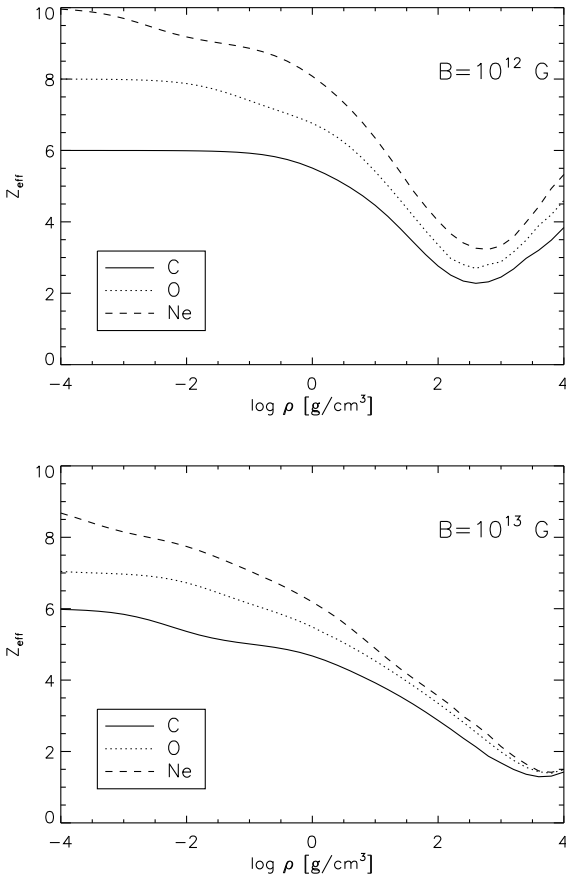


Figure 1. Effective charge Z_{eff} as a function of density for carbon, oxygen, and neon plasmas at $B = 10^{12}$ G (top) and $B = 10^{13}$ G (bottom) and $T = 3 \times 10^6$ K.

pressure components in Figure 3. The total pressure roughly follows the ion fraction curves in Figure 1. The total pressure decreases with density until the plasma becomes more ionized by pressure ionization. At high densities (e.g., $\rho \gtrsim 10^3$ g cm $^{-3}$ for $B = 10^{12}$ G), electron degeneracy (dashed line) enhances the pressure sharply although it is partially compensated by the increasing excess pressure (dotted line). At higher magnetic fields, such transition points shift to higher density because the binding energy is increased and the degree of electron degeneracy is decreased.

For a given magnetic field strength and atmosphere composition, we produced an EOS table in the temperature range $5.4 \leq \log_{10} T \leq 7.8$ with a step-size $\Delta \log_{10} T = 0.3$ and in the density range $-7.0 \leq \log_{10} \rho \leq 5.0$ with a step-size $\Delta \log_{10} \rho = 1.0$. The tables extend to low densities in order to cover strong absorption lines which form in the shallow layers of the atmosphere.

4 OPACITIES

In this section, we briefly describe our opacity calculation. More details can be found in Mori & Hailey (2006). In a strongly-magnetized plasma, opacity becomes highly anisotropic, and radiation propagates in two normal modes: the ordinary mode (O-mode), which is mostly polarized parallel to the magnetic field, and the extraordinary mode (X-mode), which is mostly polarized perpendicular to the magnetic field (Ginzburg 1970; Mészáros 1992).

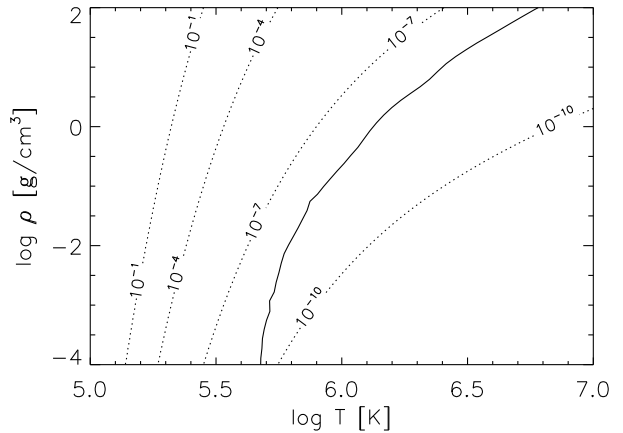


Figure 2. The fractional ratio of the C atom and C₂ molecule at $B = 10^{13}$ G (dotted lines). The solid curve is the carbon atmosphere profile with $B = 10^{13}$ G and $T_{\text{eff}} = 10^6$ K, as discussed in Section 6.

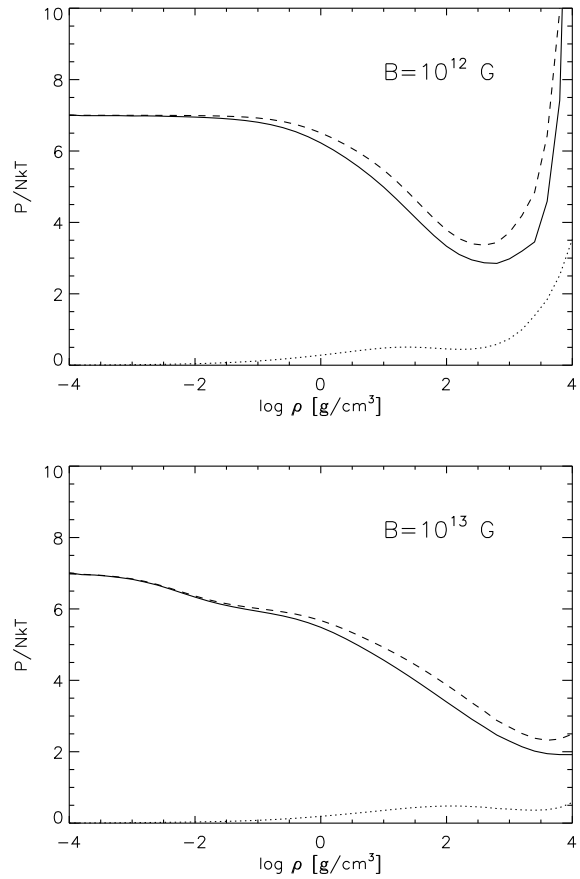


Figure 3. Normalized pressure as a function of density for a carbon plasma at $B = 10^{12}$ G (top) and $B = 10^{13}$ G (bottom) and $T = 3 \times 10^6$ K. The solid, dashed and dotted are total, ideal (electron+ion) and excess pressure. Note that we plot the magnitude of the excess pressure since it is negative.

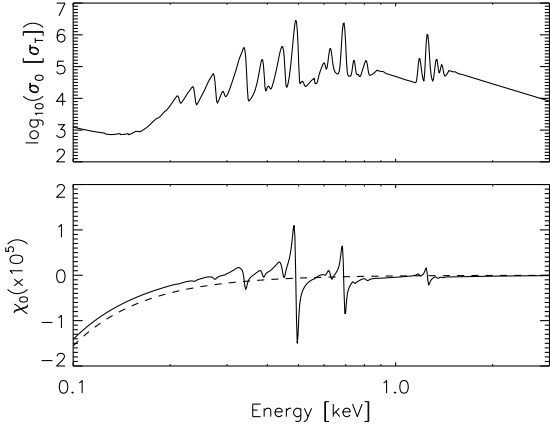


Figure 4. Cross-section (top), in units of Thomson cross-section, and polarizability tensor (bottom) as a function of energy in the $\alpha = 0$ mode for carbon at $B = 10^{12}$ G, $T = 5 \times 10^5$ K and $\rho = 10^{-2}$ g cm $^{-3}$. The dashed line shows the polarizability tensor for a fully-ionized plasma. The dominant ionization states are Li-like and Be-like carbon.

For a given density and temperature, the opacity (in cm 2 g $^{-1}$) in the normal mode j is given by

$$\kappa^j(E, \theta) = \sum_{\alpha} |\vec{e}_\alpha^j(E, \theta)|^2 \kappa_{\alpha}(E), \quad (2)$$

where $|\vec{e}_\alpha^j|$ is the polarization eigenvector; $|\vec{e}_\alpha^j|$ reflects the dielectric properties of the magnetized plasma and depends on the angle between the magnetic field and the direction of photon propagation θ , such that $\vec{e}_0^j = \vec{e}_z^j$ is the z -component (along B) of the mode eigenvector and $\vec{e}_{\pm}^j = (\vec{e}_x^j \pm i\vec{e}_y^j)/\sqrt{2}$ are the circular components.

Since mid-Z element atmospheres are usually not fully-ionized, we include the effects of bound species by using of the Kramers-Kronig relation (Bulik & Pavlov 1996; Potekhin et al. 2004). Figure 4 shows the cross-section and polarizability tensor in the $\alpha = 0$ mode when carbon is partially-ionized ($Z_{\text{eff}} = 2.9$). The cross-section (σ_0) is dominated by bound-bound and bound-free transitions in the X-ray band. The polarizability tensor (χ_0) deviates significantly from that in a fully-ionized plasma, particularly near the strong lines.

When the degree of ionization increases, the difference between using the polarizability tensors for partial ionization (complete model) and full ionization (hybrid model) becomes smaller. Figure 5 shows the X-mode opacity of carbon at $B = 10^{12}$ G in the complete and hybrid models for a nearly fully-ionized case ($Z_{\text{eff}} = 5.8$). Although the overall difference is tiny, there are noticeable deviations in the vicinity of the strong bound-bound transition lines at $E \sim 0.6$ keV (see inset). Our results indicate that the strength and shape of strong absorption lines can be strongly affected even when the plasma is nearly fully-ionized.

We produced opacity tables for the same temperature and density grids as the EOS tables. For a given set of temperature and density, our opacity tables consist of cross-sections $\sigma_{\alpha}(E)$ and polarizability tensors $\chi_{\alpha}(E)$ in the three cyclic polarization modes ($\alpha = 0, \pm 1$). We adopted ~ 2500 equal logarithmically-spaced energy grid points; this allows us to resolve narrow lines.

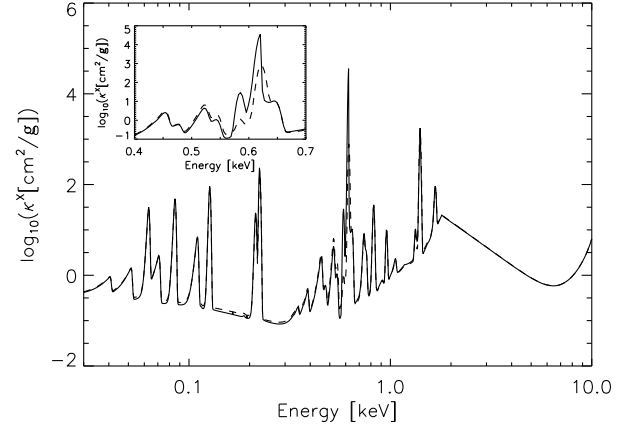


Figure 5. X-mode opacity of carbon at $B = 10^{12}$ G, $T = 2 \times 10^6$ K, $\rho = 10^{-2}$ g cm $^{-3}$, and $\theta = 10^\circ$. The solid and dashed lines show the X-mode opacity for the complete and hybrid models, respectively. The fraction of bare and H-like carbon is 81 and 19%, respectively, while other ionization species have fractions less than 0.01%. The inset is a magnified view of the $E = 0.4$ –0.7 keV region to illustrate the difference between the complete and hybrid models in the vicinity of the strongest bound-bound transition line at ~ 0.6 keV.

5 RADIATIVE TRANSFER

Thermal radiation from a NS is mediated by an atmosphere (with scale height ~ 1 cm) that covers the stellar surface. To determine the emission properties of a magnetized atmosphere, the radiative transfer equations for the two coupled photon polarization modes are solved (see Ho & Lai 2001; Ho et al. 2003, for details on the construction of the atmosphere models). We note here a few particulars of our models.

The EOS tables for a given magnetic field are arranged by temperature and density. The pressure at Thomson depth τ [= $-\kappa_0^{\text{es}} \int \rho dz$, where $\kappa_0^{\text{es}} = (Z/A)\sigma_{\text{T}}/m_p$, the atomic mass number is A , and the Thomson cross-section is σ_{T}] is calculated from hydrostatic equilibrium. With a given temperature profile, we search the EOS tables for the nearest temperatures and gas pressures and do a weighted average to obtain the density profile. To include radiation pressure P_{rad} , we calculate P_{rad} from its contribution to hydrostatic equilibrium (Mihalas 1978)

$$\frac{dP_{\text{rad}}}{d\tau} = \frac{\sigma_{\text{SB}} T_{\text{eff}}^4}{c} \frac{\kappa^{\text{F}}}{\kappa_0^{\text{es}}}, \quad (3)$$

where

$$\kappa^{\text{F}} = \frac{1}{F} \sum_j \int_0^{\infty} dv \int d\Omega \kappa_j^{\text{tot}} F_j, \quad (4)$$

F_j is the specific flux for mode j , and F is total flux; this contribution is usually small (see Section 6.1). The radiation pressure is then subtracted from the total pressure to obtain the gas pressure.

The self-consistency of the atmosphere model is determined by requiring that the fractional temperature corrections $\Delta T(\tau)/T(\tau) \ll 1\%$ at each Thomson depth, deviations from radiative equilibrium $\ll 1\%$, and deviations from constant total flux $< 1\%$. Note that the atmosphere models formally have a dependence, through hydrostatic balance, on the surface gravity g [= $(1 + z_g)GM/R^2$] and thus the NS mass M and radius R ; however, the emergent spectra do not vary much using different values of g around 2×10^{14} cm s $^{-2}$ (see Section 7.3; see also Pavlov et al.

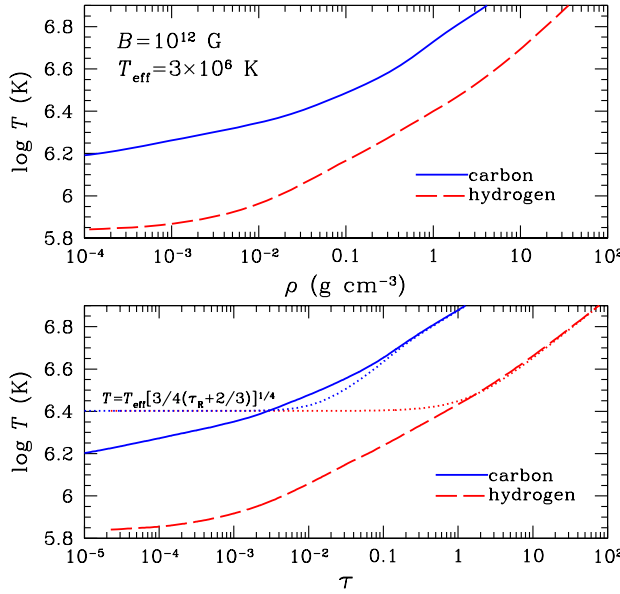


Figure 6. Temperature profiles of carbon (solid lines) and hydrogen atmospheres (dashed lines) with $B = 10^{12}$ G and $T_{\text{eff}} = 3 \times 10^6$ K. The dotted lines are grey profiles. τ is the Thomson depth and τ_R is the Rosseland depth. At large τ , temperature profiles merge with grey profiles.

1995). Most of our models are constructed using a surface gravity $g = 2.4 \times 10^{14}$ cm s $^{-2}$ with $M = 1.4M_{\odot}$, $R = 10$ km, and $z_g = 0.3$ (see Section 7.3 for other cases). Also, though our atmosphere models can have a magnetic field at an arbitrary angle Θ_B relative to the surface normal, most of the models considered in Section 7 have the magnetic field aligned perpendicular to the stellar surface ($\Theta_B = 0^\circ$; see Sections 7.3 and 8.2 for other cases). The spectra represent emission from a local patch of the NS surface.

6 ATMOSPHERE PROFILE

Figures 6 and 7 show the temperature profiles of carbon atmospheres in comparison with those of partially ionized hydrogen atmospheres at $B = 10^{12}$ G and $B = 10^{13}$ G. There are two distinct differences between hydrogen and mid-Z element atmosphere profiles; these differences are due to the fact that bound-bound and bound-free opacities are more important than free-free opacities. Temperature profiles in the mid-Z element atmospheres are closer to grey than in hydrogen atmospheres since the opacities are less energy-dependent, while the free-free opacity (which is dominant in hydrogen atmospheres) has a steep energy dependence. Photosphere densities are also significantly smaller since opacities are higher than in hydrogen atmospheres, and photosphere densities increase with magnetic field since opacities are reduced.

Figure 8 shows the effective charge of carbon atmospheres at different optical depths. At $B = 10^{12}$ G and $T_{\text{eff}} \gtrsim 3 \times 10^6$ K, the H-like carbon ion is largely populated. At higher B and lower T_{eff} , various ionization states exist in the atmosphere, and they are likely to produce numerous spectral features. Figure 9 illustrates where X-mode and O-mode photons decouple from the matter as a function of energy. It is clear that X-mode photons come from deeper, hotter layers in the atmosphere than O-mode photons; therefore spectra are strongly polarized and dominated by the X-mode photons.

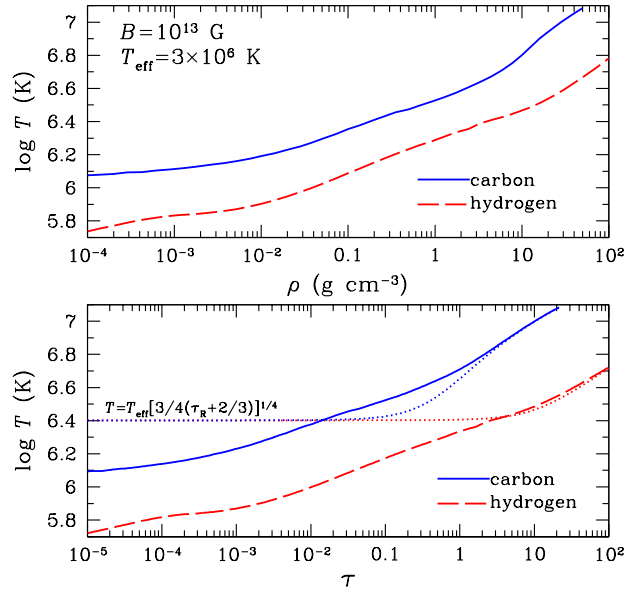


Figure 7. Temperature profiles of carbon and hydrogen with $B = 10^{13}$ G and $T_{\text{eff}} = 3 \times 10^6$ K. Notation is the same as in Figure 6.

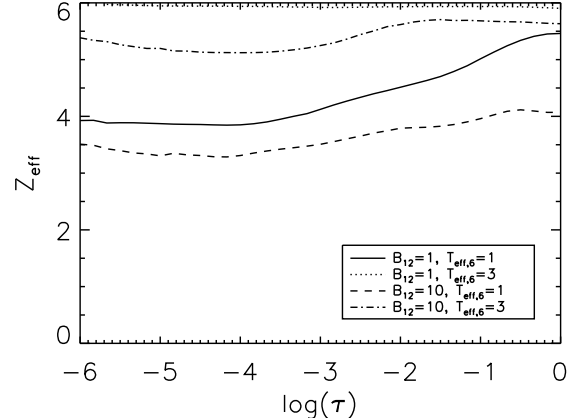


Figure 8. Effective charge of carbon as a function of Thomson depth τ at $B = 10^{12}$ G and $B = 10^{13}$ G and $T_{\text{eff}} = 10^6$ and 3×10^6 K. Carbon is nearly fully-ionized at $T_{\text{eff}} = 5 \times 10^6$ K.

6.1 Radiative levitation

At high temperature, mid-Z element ions may be levitated by radiation pressure through strong absorption lines. Our scheme described in Section 5 does not perform radiative transfer of individual lines since we compute the gradient of radiation pressure using opacities that are integrated over frequency. Although detailed line-by-line radiative transfer modeling is beyond the scope of this paper, we estimate here the effects of radiative levitation in mid-Z element atmospheres. Gravitational force on a carbon ion is 4.6×10^{-9} dyne when $g = 2.4 \times 10^{14}$ cm s $^{-2}$, while radiation force through an absorption line is $1.6 \times 10^{-11} \sigma_l (T_{\text{eff}}/10^7 \text{ K})^4$ dyne, where σ_l is the line cross-section in units of Thomson cross-section (σ_T). In the carbon atmosphere at $B = 10^{12}$ G and $T_{\text{eff}} = 5 \times 10^6$ K, several strong lines have cross-sections as large as $\sim 10^4 \sigma_T$. Therefore, radiative levitation can be important through strong absorption

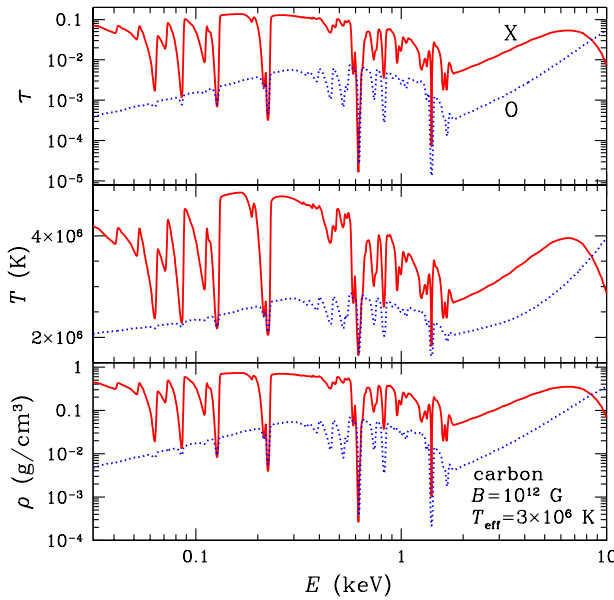


Figure 9. Thomson depth (where photons decouple from matter) as a function of energy for a carbon atmosphere with $B = 10^{12}$ G and $T_{\text{eff}} = 3 \times 10^6$ K. The bottom two panels plot the local temperature and density at the corresponding Thomson depth. The solid and dotted lines are for the X-mode and O-mode, respectively. For the two polarization modes, the photon-decoupling layer is defined such that the effective (angle-averaged) optical depth of each mode is unity. See Section 4.2 in Ho & Lai (2001) for more details on how we calculate effective optical depths.

lines at $T_{\text{eff}} \sim 5 \times 10^6$ K, while it will be negligible at lower temperatures.

6.2 Validity of LTE assumption

The LTE assumption may become invalid at low density and high temperature. To our knowledge, the validity of LTE assumption has not been investigated in previous atmosphere models for cooling NSs. Three conditions need to be fulfilled for a LTE plasma (Salzmann 1998): (1) Maxwell-Boltzmann distribution of the electron and ion velocities, (2) Saha equilibrium for the charge state distribution, and (3) Boltzmann distribution of the excited states. The first condition is well-satisfied in our case since the electron self-collision time is very short. However, the latter two conditions are usually more restrictive. We examine the second condition following Salzmann (1998). For the third condition, we estimate radiative and collisional transition rates between the ground and excited states and apply the criteria from Griem (1964).

In Figure 10, we plot the (ρ, T) regime where the LTE assumption is valid, along with carbon atmosphere profiles at $B = 10^{12}$ G and two effective temperatures. The condition for a Boltzmann distribution (hatched area) is more restrictive than the one for Saha equilibrium (grey area). We find that both conditions break down in the upper atmosphere layers with $\rho \lesssim 10^{-4}$ g cm $^{-3}$ and 10^{-3} g cm $^{-3}$ at $T_{\text{eff}} = 10^6$ K and 5×10^6 K, respectively. Therefore, only a few of the strongest lines will be affected by non-LTE effects. At higher densities, Saha equilibrium is recovered. The condition for the Boltzmann distribution (hatched area) becomes irrelevant in the (ρ, T) regime where a fraction of excited states is small (solid lines). Therefore, the LTE assumption is completely valid above

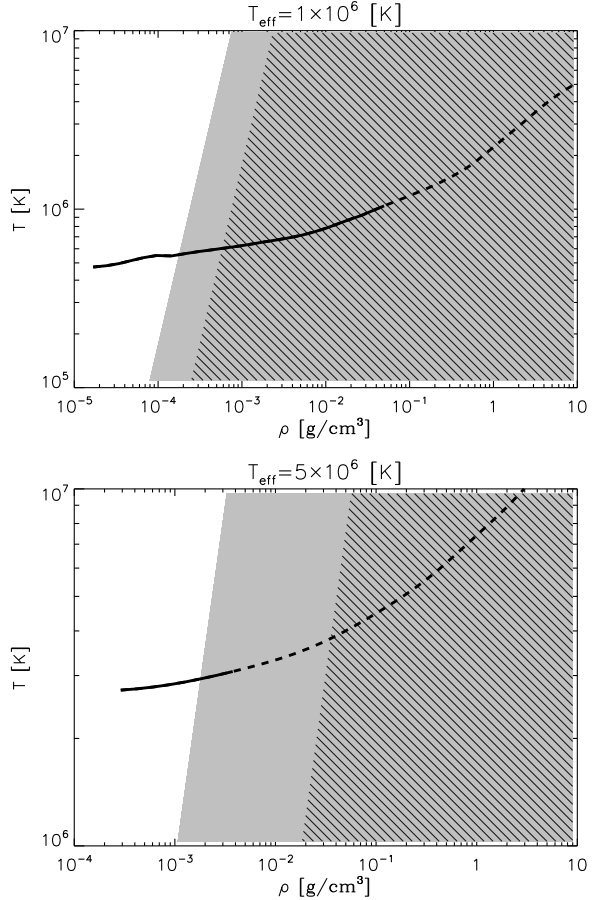


Figure 10. LTE conditions for carbon atmospheres at $B = 10^{12}$ G and $T_{\text{eff}} = 10^6$ K (top) and $T_{\text{eff}} = 5 \times 10^6$ K (bottom). The Saha equation is valid in the grey area, while the Boltzmann distribution for the excited states is valid in the hatched area. The solid + dashed curves show the temperature profile of the atmospheres. The fraction of excited states exceeds 10% on the dashed lines, while the occupation probability of the ground state is larger than 90% on the solid lines.

$\rho \sim 10^{-4}$ g cm $^{-3}$ at $T_{\text{eff}} = 10^6$ K. On the other hand, the occupation probabilities of excited states computed by using the Boltzmann distribution may not be correct in the region between $\rho \sim 4 \times 10^{-3}$ and 3×10^{-2} g cm $^{-3}$ at $T_{\text{eff}} = 5 \times 10^6$ K. We find that such a region does not exist at lower effective temperatures.

We thus expect that only a few strong absorption lines will be altered by non-LTE effects, while the bulk of the mid-Z element atmosphere structure and spectra are unaffected in our models. To address the non-LTE effects, one must find collisional-radiative steady states by solving rate equations with both radiative and collisional processes included (Salzmann 1998). Such an analysis is beyond the scope of this paper.

7 MODEL ATMOSPHERE SPECTRA

We construct spectra of mid-Z element atmospheres with $B = 10^{12}$ G and 10^{13} G and three different effective temperatures ($T_{\text{eff}} = 10^6, 3 \times 10^6$, and 5×10^6 K). The results are shown for carbon (Figures 11 and 12), oxygen (Figures 13 and 14) and neon (Figure 15 and 16). For comparison, we plot partially ionized hydrogen atmo-

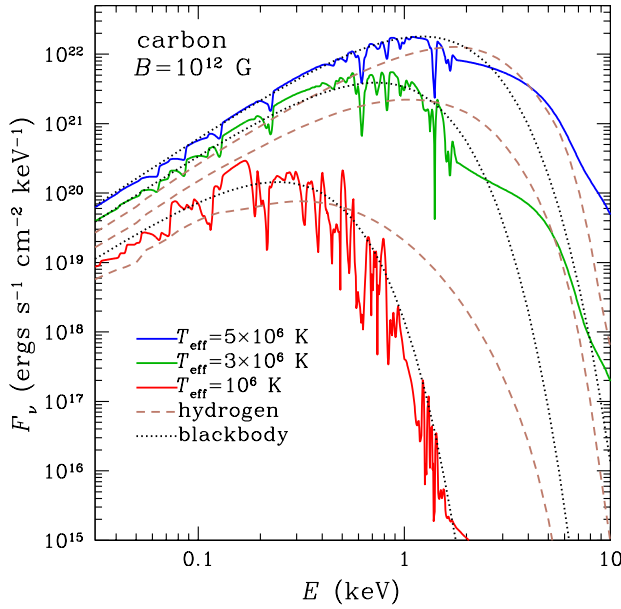


Figure 11. Spectra of carbon atmospheres with $B = 10^{12}$ G and three effective temperatures ($T_{\text{eff}} = 1, 3$ and 5×10^6 K). The dashed lines show partially ionized hydrogen atmosphere spectra with the same B and T_{eff} , and the dotted lines show blackbody spectra with $T = T_{\text{eff}}$.

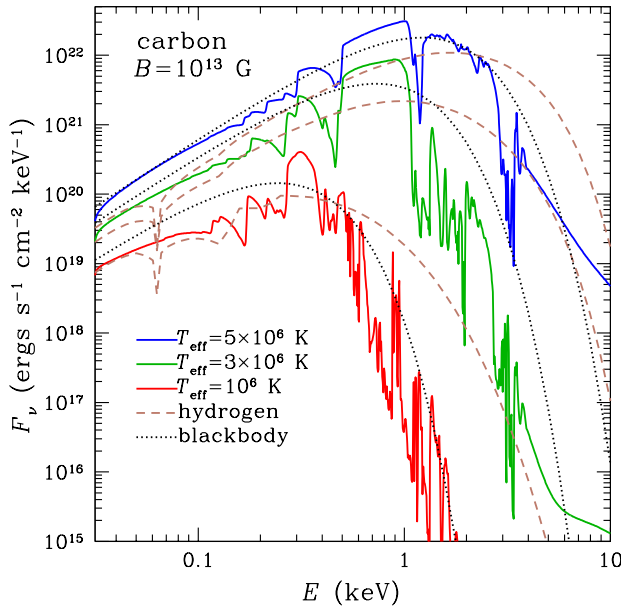


Figure 12. Spectra of carbon atmospheres with $B = 10^{13}$ G. Notation is the same as in Fig. 11.

sphere spectra (dashed lines) and blackbody spectra (dotted lines) with the same magnetic field strengths and temperatures.

7.1 Spectral energy distribution

Overall, mid-Z element atmosphere spectra are significantly softer than hydrogen atmosphere spectra (dashed lines) and close to blackbody spectra (dotted lines) because temperature profiles are

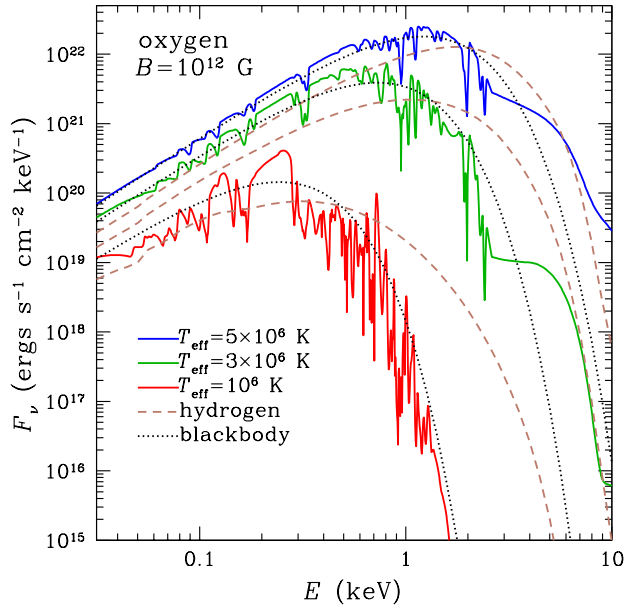


Figure 13. Spectra of oxygen atmospheres with $B = 10^{12}$ G. Notation is the same as in Fig. 11.

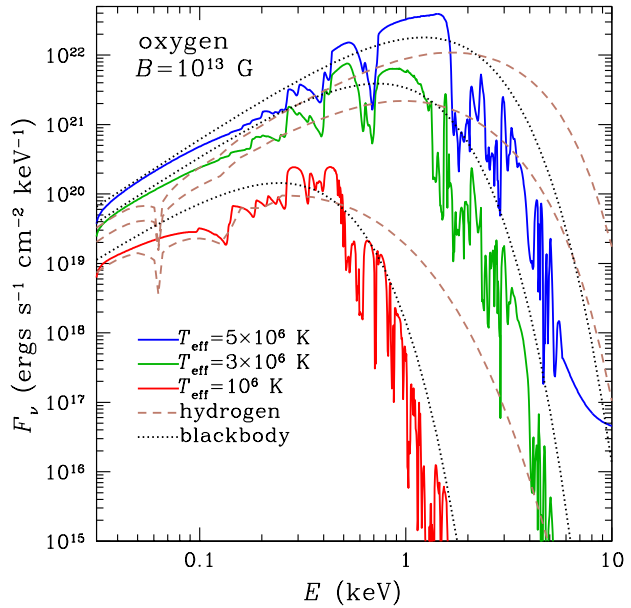


Figure 14. Spectra of oxygen atmospheres with $B = 10^{13}$ G. Notation is the same as in Fig. 11.

closer to grey. The mid-Z element atmosphere spectra are even softer than blackbody in the Wien tail due to the photo-absorption edges (at $\sim 1.5 - 2$ keV for $B = 10^{12}$ G models). The absorption edges are due to bound-free transitions from the innermost electron [$(mv) = (00)$ state] in different ionization species. At higher energy, the spectra become harder than blackbody and hydrogen atmospheres in order to maintain radiative equilibrium. A similar feature is seen in the magnetized iron atmosphere models of Rajagopal et al. (1997). This appears to be a common signature of heavy element atmospheres over a large range of B and T_{eff} .

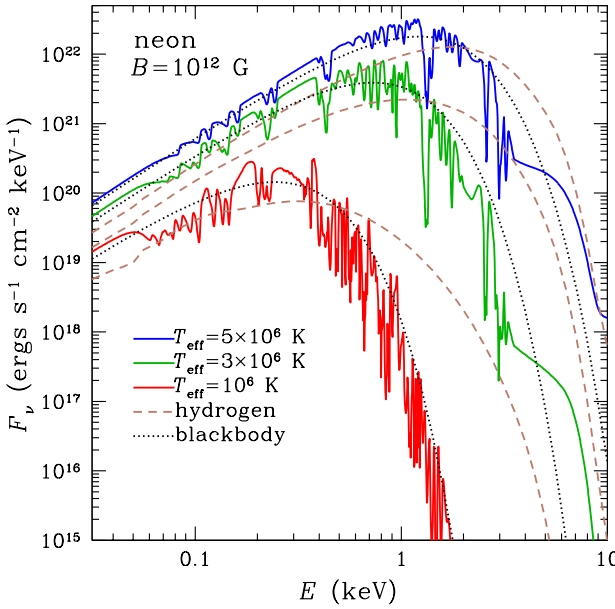


Figure 15. Spectra of neon atmospheres with $B = 10^{12}$ G. Notation is the same as in Fig. 11.

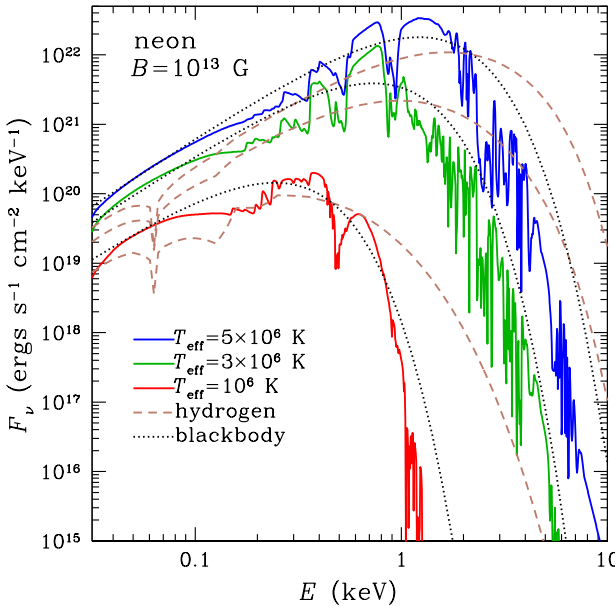


Figure 16. Spectra of neon atmospheres with $B = 10^{13}$ G. Notation is the same as in Fig. 11.

7.2 Absorption features

Numerous absorption lines are present, especially in low temperature models, and as expected, heavier element atmospheres show more absorption features. Magnetic field dependence is also remarkable. There are more discrete absorption lines at $B = 10^{12}$ G than at $B = 10^{13}$ G. Most of the absorption lines at $B = 10^{12}$ G are longitudinal transitions ($\Delta m = 0, \Delta v > 0$ in the $\alpha = 0$ mode). On the other hand, the longitudinal transitions become significantly weaker at higher B because the $\alpha = 0$ component of the polarization

vector components in the X-mode becomes smaller with increasing B . This effect is most noticeable in the low temperature models (e.g., see the neon models at $T_{\text{eff}} = 10^6$ K). The suppression of longitudinal transitions is also seen in magnetized hydrogen atmospheres (Ho et al. 2003). Note that longitudinal transitions appear strong in the mid-Z element atmospheres at $B = 10^{12}$ G since the magnetic field is not as dominant over the nuclear Coulomb field at $\beta_Z \gtrsim 1$.

In the $B = 10^{13}$ G model spectra, it is mainly the transverse transition lines that are visible. At $B = 10^{13}$ G, $\Delta m = +1, \Delta v = 0$ transitions from bound electrons in outer shells are strong (e.g., lines at $\sim 0.26, 0.39, 0.69$ and 1.8 keV in oxygen atmosphere models at $B = 10^{13}$ G). The lines appear at lower energies when the temperature is lower and oxygen is less ionized (compare oxygen spectra at $T_{\text{eff}} = 10^6$ K and 3×10^6 K for $B = 10^{13}$ G in Figure 14). Other weaker and broader transverse transition lines ($\Delta m = \pm 1, \Delta v > 0$) are also present in the $B = 10^{13}$ G model spectra.

Most absorption lines have asymmetric profiles with low energy tails due to motional Stark effects. Some of the strong lines show more complex profiles due to the enhanced polarizability near the lines. In general, line widths become larger at higher magnetic fields since motional Stark effects are more important. Only photo-absorption edges from the innermost electrons are clearly visible at high energy where there are no bound-bound transition lines (e.g., $E \gtrsim 1.7$ keV for carbon atmosphere spectra at $B = 10^{12}$ G), although bound-free transitions are important throughout the X-ray band.

7.3 Dependence on magnetic field geometry and surface gravity

Here we illustrate the dependence of the atmosphere models on magnetic field geometry (Θ_B) and surface gravity (g). Figure 17 shows temperature profiles and carbon atmosphere spectra at two different magnetic field angles (Θ_B) with respect to the NS surface normal. There is no remarkable difference between the two magnetic field orientations, except at several strong lines and the photo-ionization edges at high energy ($E \gtrsim 1.7$ keV for carbon at $B = 10^{12}$ G). The angular dependence shown here reflects the (rotational) phase variation of atmosphere spectra, as the observer sees regions of the NS surface with different magnetic field orientations (see Section 8.2).

Atmosphere emission can also be highly beamed in the presence of a magnetic field (Shibanov et al. 1992; Pavlov et al. 1994). Figure 18 shows the energy-dependent beam pattern for the atmosphere models with $T_{\text{eff}} = 3 \times 10^6$ K and $B = 10^{12}$ and 10^{13} G. Note that the emission is more beamed at higher magnetic fields. There are some noticeable differences between hydrogen and mid-Z element atmospheres. Our results show that energy-resolved lightcurve analysis can potentially be used as a diagnostic tool to determine the surface composition.

Figure 19 shows carbon spectra at two rather extreme values of g ($= 5 \times 10^{13}$ and 5×10^{14} cm s $^{-2}$) and hence NS mass and radius (see, e.g., Lattimer & Prakash 2001). Our results show mid-Z element atmosphere spectra, like magnetic hydrogen spectra (see, e.g., Pavlov et al. 1995), have a weak dependence on gravitational acceleration. This is contrary to the results of unmagnetized NS atmosphere spectra in which several absorption features vary in their strengths and shapes strongly with g (Zavlin et al. 1996). The weak dependence on g is partially due to the fact that spectral features in mid-Z element atmospheres are primarily broadened by motional Stark effects (which are independent of plasma density) and pres-

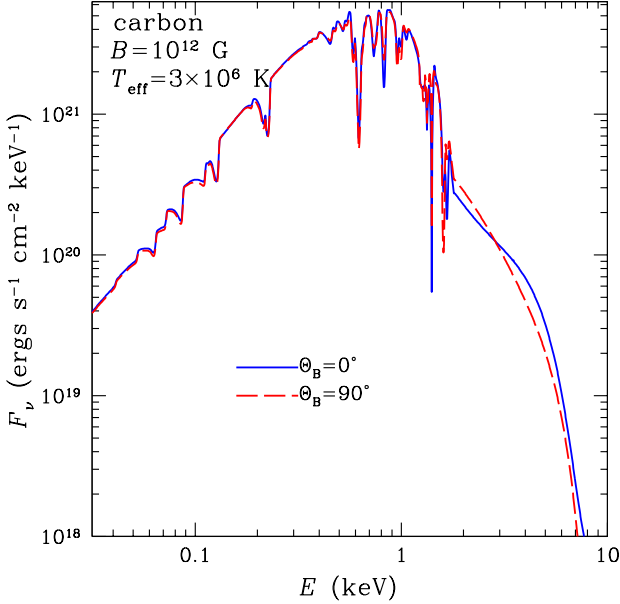
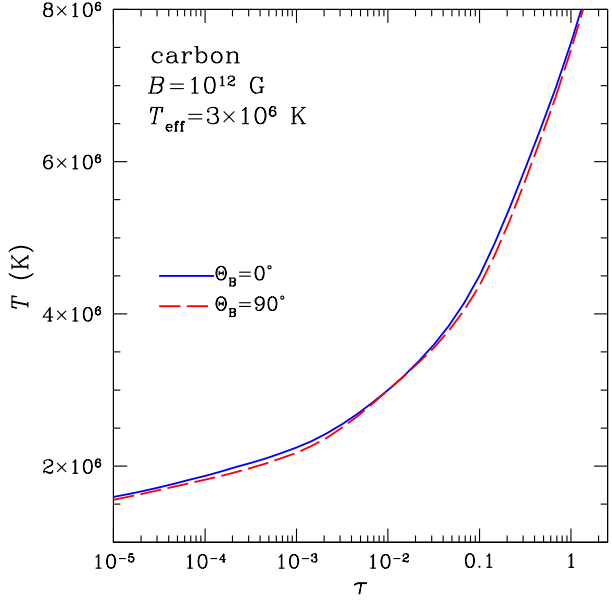


Figure 17. Temperature profile (top) and carbon atmosphere spectra (bottom) with $\Theta_B = 0^\circ$ (solid lines; magnetic field perpendicular to the atmosphere plane) and $\Theta_B = 90^\circ$ (dashed lines; magnetic field parallel to the atmosphere plane). The other parameters are set to $B = 10^{12}$ G and $T_{\text{eff}} = 3 \times 10^6$ K.

sure effects are small (since absorption lines are formed at low density).

8 X-RAY SPECTROSCOPY AND DETERMINATION OF NEUTRON STAR PARAMETERS

Given the results in the previous sections, it is useful to consider what one can learn from X-ray spectroscopy of INSSs, especially those which show absorption features in their spectra. Four NS parameters are important in determining thermal spectra; surface composition (Z), magnetic field (B), effective temperature (T_{eff}),

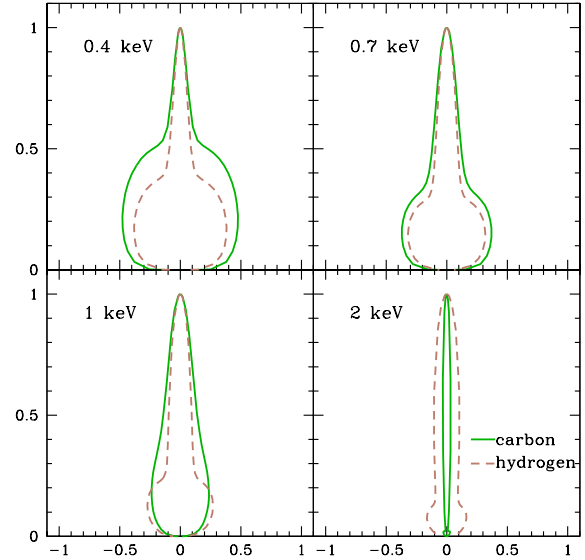


Figure 18. Polar diagrams of the specific intensity (scaled to the intensity in the normal direction) from the carbon (solid lines) and hydrogen (dashed lines) atmosphere models with $T_{\text{eff}} = 3 \times 10^6$ K and $B = 10^{12}$ G (top) and $B = 10^{13}$ G (bottom).

and gravitational redshift (z_g). It is desirable to detect multiple spectral features to break degeneracies between the parameters. We discuss here the feasibility of measuring these NS parameters with X-ray spectroscopy.

8.1 Surface composition

Given the substantial differences in spectral energy distribution (SED) and absorption features, it should be relatively easy to distinguish between mid-Z element and hydrogen atmospheres. In particular, a possible signature for the presence of a mid-Z element atmosphere is the detection of multiple strong absorption lines at high

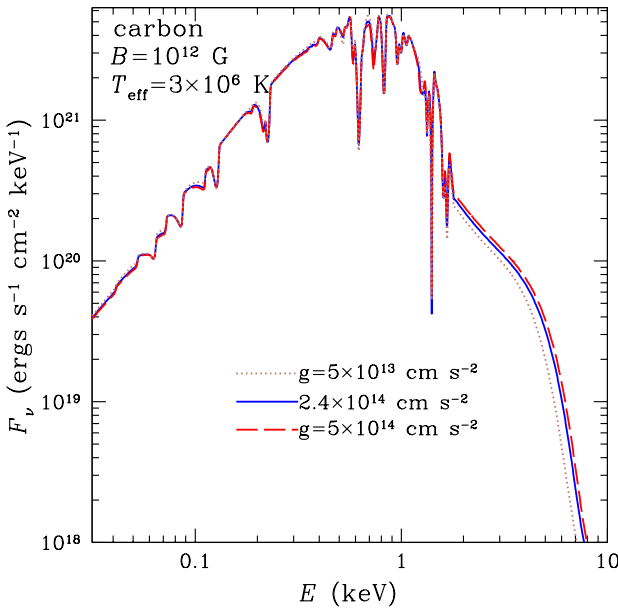
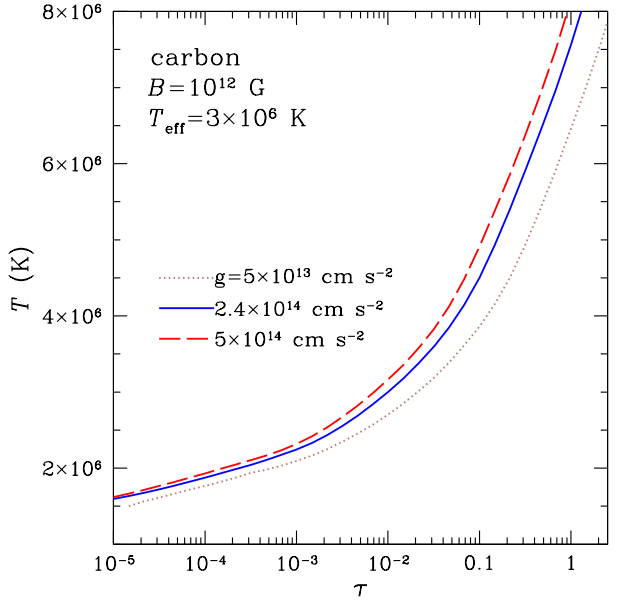


Figure 19. Temperature profiles (top) and carbon atmosphere spectra (bottom) with $g = 5 \times 10^{13}$ (dotted lines), 2.4×10^{14} (solid lines), and $5 \times 10^{14} \text{ cm s}^{-2}$ (dashed lines), corresponding to $(M,R) = (0.5M_{\odot}, 12 \text{ km})$, $(1.4M_{\odot}, 10 \text{ km})$, and $(2.2M_{\odot}, 10 \text{ km})$, respectively. The other parameters are set to $B = 10^{12} \text{ G}$, $T_{\text{eff}} = 3 \times 10^6 \text{ K}$, and $\Theta_B = 0^\circ$.

energy ($E \gtrsim 1 \text{ keV}$). Multi-wavelength SED analysis over optical and X-ray bands will be useful since mid-Z element atmospheres are significantly softer than hydrogen atmospheres (Pavlov et al. 1996). Since the number of absorption features and their energies are strongly dependent on the surface composition, it is possible to distinguish between carbon and oxygen atmospheres if multiple spectral features are detected.

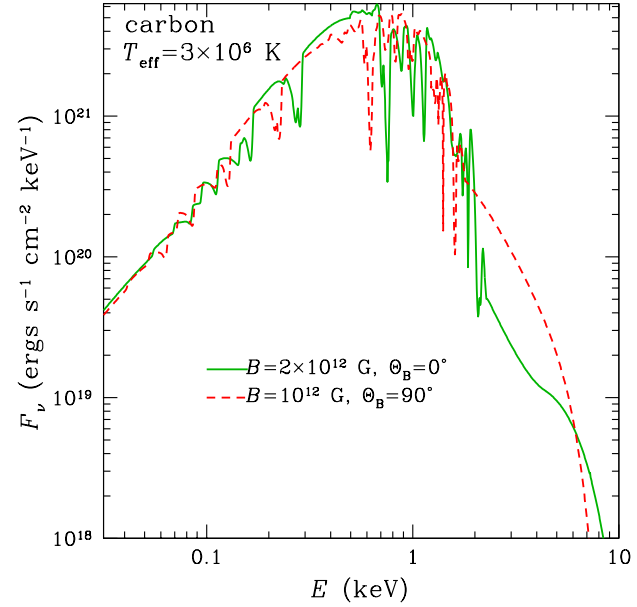


Figure 20. Carbon atmosphere spectra with $B = 2 \times 10^{12} \text{ G}$ and $\Theta_B = 0^\circ$ (solid line) and $B = 10^{12} \text{ G}$ and $\Theta_B = 90^\circ$ (dashed line). In both cases, $T_{\text{eff}} = 3 \times 10^6 \text{ K}$. The former and latter cases correspond to atmosphere spectra from the pole and equator in a dipole magnetic field configuration, respectively.

8.2 Magnetic field

The absorption features shown in Figures 11–16 are deeper and narrower than the observed spectral features from INSSs (Sanwal et al. 2002; Haberl et al. 2003, 2004b; van Kerkwijk et al. 2004). This is partly due to the fact that our atmosphere models are constructed with a single magnetic field strength B and orientation Θ_B , thus reflecting emission from a local patch on the NS surface. The absorption features in our model spectra will appear broadened if there are magnetic field variations over the surface. We expect to see dramatic changes in the spectra even with a small magnetic field difference, since the ionization fraction and line energies depend strongly on B . Figure 20 shows carbon atmosphere spectra at two magnetic field strengths and angles, corresponding to the pole and equator for a magnetic dipole configuration. Indeed, atmosphere spectra can look quite different merely due to a factor of two difference in the magnetic field strength. Thus thermal spectra of INSSs can show significant rotational phase-variation due to a magnetic field distribution, even when the surface temperature is uniform.

In order to construct synthetic atmosphere spectra, one must integrate emission from patches of the NS surface with differing B , Θ_B , and T_{eff} . Such synthetic spectra are necessarily model-dependent (see, e.g., Zavlin et al. 1995; Zane et al. 2001; Ho & Lai 2004; Zane & Turolla 2006; Ho et al. 2007), as the magnetic field and temperature distributions over the surface are unknown. Although magnetic field broadening is different for each absorption line, atomic line energies vary approximately by $\Delta E/E \simeq 10\%$ and 30% for a factor of 1.5 and 2 variation in magnetic field strength. Electron or ion cyclotron lines may appear in the X-ray band when B is lower or higher than the values considered in this paper. Some of the observed absorption features have been attributed to cyclotron lines (Haberl et al. 2003). Since cyclotron line energy varies linearly with B , we expect cyclotron lines to be

broader and have larger phase variation than atomic lines. Therefore, line width analysis can be a useful diagnostic tool to probe the magnetic field distribution over the NS surface, given that the intrinsic widths of absorption lines are narrow in mid-Z element atmospheres (Mori & Hailey 2006). Magnetic field variation can smear out narrow absorption lines and reduce the accuracy of determining other NS parameters such as the gravitational redshift. Phase-resolved spectroscopy is essential to disentangle magnetic field effects from the other parameters and to probe the magnetic field geometry.

8.3 Effective temperature

The effective temperature must be measured to constrain the cooling history of NSs (Page et al. 2004; Yakovlev & Pethick 2004). Thermal spectra of most INSSs are fit with either blackbody or fully-ionized hydrogen atmosphere models, each of which exhibits the softest and hardest spectra, respectively. Therefore, errors in the measured effective temperatures are primarily due to uncertainty in the surface composition.

Although mid-Z element atmospheres can have overall SEDs close to a blackbody, there are several significant differences from blackbody spectra. In the Wien tail, mid-Z element atmosphere spectra are softer than a blackbody due to photo-absorption lines and edges and become harder than a blackbody at higher energy. Therefore the effective temperature can be higher than the blackbody temperature if high energy tails are not fully covered by X-ray spectroscopy. Alternatively, the high energy part of X-ray spectra may be erroneously fit by an additional blackbody component (see Section 9.1 for the case of 1E1207). It is important to cover a wide energy band and fit the data with model atmosphere spectra, rather than fitting with one or two blackbody components and simple Gaussian or Lorentzian absorption lines.

8.4 Neutron star mass and radius

One of the ultimate goals in NS research is to uniquely determine the mass and radius of NSs and constrain the nuclear equation of state of the NS core. In X-ray spectroscopy, gravitational redshift z_g is one of the NS parameters which can be measured once X-ray data are fit with model atmosphere spectra. The accuracy of a gravitational redshift measurement is limited by magnetic field surface variations since line energies change with both B and z_g . To increase accuracy, phase-resolved spectroscopy is essential because B varies with rotation phase but z_g does not. Grating spectroscopy will measure gravitational redshift with high accuracy if magnetic field variation is not so severe and photon statistics is good. In the future, high-resolution spectroscopy missions, such as *Constellation-X*, will be able to measure the magnetic field and gravitational redshift with unprecedented accuracy.

It is possible to measure the surface gravity (g) from line widths if the lines are primarily broadened by pressure effects (Paelens 1997). However, motional Stark effects produce line broadening far larger than pressure effects; this is partly because lines are formed in low density layers. Also, our study indicates that it is difficult to measure surface gravity from overall spectral fitting since mid-Z element spectra have a very weak dependence on g (see Figure 19). Therefore, the methods for constraining g by using absorption features is applicable only to weakly-magnetized NSs ($B \lesssim 10^9$ G) since their spectra are nearly free from the magnetic field effects discussed in this paper (see also Zavlin et al. 1996).

On the other hand, it may be possible to constrain g in heavier element atmospheres (e.g., Fe) since motional Stark effects are further reduced while ion-coupling effects are enhanced. We plan to investigate heavy element atmospheres composed of silicon and iron in future work.

Radius measurements are feasible by combining X-ray spectroscopy (which measures flux) and distance measurements. Distances to several nearby INSSs have been measured with relatively high accuracy by parallax measurements (Walter & Lattimer 2002; Kaplan et al. 2002; van Kerkwijk & Kaplan 2006). However, it should be kept in mind that only a fraction of the surface (such as hot spots) may be visible due to temperature anisotropy caused by strong magnetic fields (Greenstein & Hartke 1983; Geppert et al. 2004, 2006). Independent lightcurve analysis will be helpful to determine the size of the emission region.

9 COMPARISON WITH X-RAY DATA OF ISOLATED NEUTRON STARS

In this section, we discuss INSS thermal spectra in the context of mid-Z element atmospheres. We consider the INSS 1E1207.4–5209 and the class of radio-quiet INSSs; these all show spectral features in their X-ray spectra, except RX J1856.5–3754. Table 1 summarizes their observational properties based on recent *Chandra* and *XMM-Newton* observations.

9.1 1E1207.4–5209

1E1207 is a hot isolated NS² with an age $\sim 7 \times 10^3$ y. Remarkably, it shows two broad absorption features at ~ 0.7 and ~ 1.4 keV and an excess above blackbody emission at $\gtrsim 2$ keV. A second blackbody component with a small emitting area ($R \lesssim 1$ km) and high temperature ($T \gtrsim 3 \times 10^6$ K) has been used to fit the high energy excess (Mereghetti et al. 2002; Bignami et al. 2003; De Luca et al. 2004; Mori et al. 2005). However, it is puzzling that the pulsed fraction is not particularly large at high energies (De Luca et al. 2004), while small hot spots can strongly modulate X-ray lightcurves. Also, the temperature can be quite different depending on the number of continuum components used to fit the data, e.g., $kT_{BB}=260$ eV when using a single blackbody and $kT_{BB}=150$ eV when using a double blackbody (the second blackbody in the latter case has ~ 300 eV; Mori et al. 2005).

Proposed models involving cyclotron lines or atomic lines from a light element (H, He) atmosphere (Sanwal et al. 2002; Bignami et al. 2003; Turbiner & López Vieyra 2004) seem unlikely since line strengths are significantly weakened by vacuum resonance effects (Ho & Lai 2004; van Adelsberg & Lai 2006, and references therein) or the ionization states responsible for the observed lines are not abundant (Mori & Hailey 2006). Alternatively, Hailey & Mori (2002) and Mori & Hailey (2006) proposed a mid-Z element atmosphere for 1E1207.

Figure 21 shows the *XMM-Newton*/EPIC-PN spectrum of 1E1207 and the oxygen atmosphere spectrum with $B = 10^{12}$ G, $T_{eff} = 4 \times 10^6$ K and $z_g = 0.4$; the latter is convolved with the *XMM-Newton* EPIC energy resolution. Although many of the narrow absorption lines are blended or smeared out, some substructure

² Recent timing analysis suggests that 1E1207 is in a binary system (Woods et al. 2006). However, it is unlikely that 1E1207 is an accreting NS.

Table 1. Summary of X-ray observations of selected INSSs

Object	kT_{BB} [eV]	B_d [10^{13} G]	E_{line} [keV]	σ [eV]	EW [eV]
1E1207.4–5209 ^(a)	260	?	0.7, 1.4	130, 76	100, 60
RBS 1774	102	< 24	0.75	27	27
RX J1308.6+2127	103	3.4	0.23, 0.46	150, 260	200, 180
RX J1605.3+3249	96	?	0.40, 0.59, 0.78	87 ^(f)	96, 76, 67
RX J0806.4–4123 ^(b)	96	< 14	0.43	70 ^(f)	33
RX J0720.4–3125 ^(c)	85–95	2.4	0.28	90	0–70
RX J1856.5–3754	62	~ 1 ^(d)	—	—	—
RX J0420.0–5022 ^(e)	45	< 18	0.33	70 ^(f)	45

NOTES:

We list blackbody temperature (T_{BB}), dipole magnetic field strength (B_d), line energy, line width, and equivalent width of the observed absorption features. All the temperatures were measured by assuming a single blackbody component. The observed absorption lines were fit with a Gaussian line profile and σ refers to the Gaussian line width defined in equation (1) of Mori et al. (2005). The line parameters are subject to the choice of continuum models (Mori et al. 2005) and the number of fitted lines (Haberl 2006). See Haberl (2006) for a complete reference list of the observations.

(a) The source shows an excess above a blackbody at $E \gtrsim 2$ keV; an additional continuum component has been used to fit this excess (Mori et al. 2005).

(b) An additional absorption feature may be present at higher energy, and spectral fitting with two lines yields $E_{line} = 0.31$ and 0.61 keV (Haberl 2006).

(c) Over the last six years, X-ray spectra of RXJ0720 have become harder, and the line strength has increased (de Vries et al. 2004; Vink et al. 2004; Haberl et al. 2006).

(d) Dipole magnetic field strength was estimated from the $H\alpha$ nebula in the vicinity of RX J1856.5–3754 (van Kerkwijk & Kulkarni 2001; Kaplan et al. 2002).

(e) Based on the 20 ksec *XMM-Newton* EPIC-PN data, Haberl et al. (2004a) indicated an absorption feature at $E = 0.33$ keV. However, its significance is not definitive yet (Haberl 2006), and our independent analysis of the *XMM-Newton* data has not confirmed a significant spectral feature.

(f) The line width was fixed while fitting the spectra.

is still seen. Remarkably, the oxygen atmosphere spectrum in Figure 21 exhibits the three spectral features seen in the 1E1207 spectrum (i.e., two broad absorption features at ~ 0.7 and 1.4 keV and spectral hardening above ~ 2 keV). See Table 1 in Mori & Hailey (2006) for identification of the bound-bound transitions responsible for the 0.7 and 1.4 keV features and their unredshifted line energies. In our convolved model spectrum, the 0.7 keV feature shows a more complex structure than the 1.4 keV feature because there are more blended absorption lines at ~ 0.7 keV. Indeed, some analyses of the *XMM-Newton*/EPIC data of 1E1207 indicate the presence of substructure at ~ 0.7 keV (Mereghetti et al. 2002; Mori & Hailey 2006). The edge-like feature in the model spectrum at ~ 2 keV (similar to the excess above a blackbody in the 1E1207 spectrum) is due to bound-free transitions from the innermost electron in the $(mv) = (00)$ state of various oxygen ions. In the 1E1207 spectra, there is an indication of an additional absorption feature at $E \lesssim 0.3$ keV, where the oxygen atmosphere spectrum also shows an absorption line. Given the less reliable instrumental calibration and stronger effects of interstellar absorption at low energies, we plan to more carefully investigate the significance of this potential absorption feature in future work.

Note that the model atmosphere spectrum shown here is not completely realistic because we have not taken into account the distribution of magnetic field and temperature over the surface (see Sections 7.3 and 8.2). More detailed analysis based on spectral fitting by varying NS atmosphere parameters and viewing geometries is in progress. Given the good photon statistics with the 260 ksec *XMM-Newton* data (Bignami et al. 2003; Mori et al. 2005) and the three (or possibly four) spectral features to fit, we are optimistic about pinning down the surface composition, magnetic field, temperature, and gravitational redshift of 1E1207 with the existing CCD spectral data.

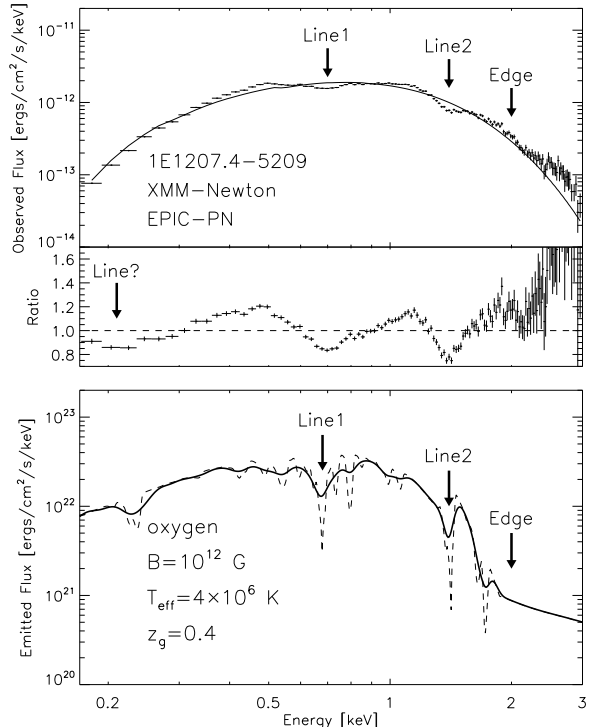


Figure 21. Unfolded *XMM-Newton* EPIC-PN spectrum of 1E1207.4–5209 (top) and spectra of oxygen atmosphere with $B = 10^{12}$ G, $T_{eff} = 4 \times 10^6$ K and $z_g = 0.4$ (bottom). In the top panel, we overlaid a blackbody spectrum to illustrate the absorption features; we also show the ratio of the data and blackbody. There is potentially another absorption feature at $E \lesssim 0.3$ keV (indicated by an arrow in the ratio plot). In the bottom panel, the solid line is the model atmosphere spectrum convolved with the *XMM-Newton* EPIC-PN energy resolution, while the dashed line is the raw spectrum.

9.2 Radio-quiet neutron stars

Seven nearby INS are characterized as radio-quiet NSs (RQNSs) since they exhibit similar spectral and timing properties (van Kerkwijk & Kaplan 2006). At least five of them show a single or multiple absorption features at $E \simeq 0.2 - 0.7$ keV (Haberl et al. 2003; van Kerkwijk et al. 2004; Haberl et al. 2004b; Zane et al. 2005; Schworer et al. 2005; Haberl 2006), while the brightest INS RX J1856.5–3754 shows a nearly perfect blackbody spectrum without any spectral features (Burwitz et al. 2003). Some of the observed absorption features have been interpreted as proton cyclotron lines or hydrogen/helium atomic lines at $B = 10^{13} - 10^{14}$ G (van Kerkwijk & Kaplan 2006). Timing analyses yield similar dipole magnetic field strengths (Kaplan & van Kerkwijk 2005a,b).

Figure 22 shows the *XMM-Newton*/EPIC-PN spectrum of RX J1605.3+3249 and the oxygen atmosphere spectrum with $B = 10^{13}$ G, $T_{\text{eff}} = 1.5 \times 10^6$ K and $z_g = 0.4$; the latter is convolved with *XMM-Newton* EPIC energy resolution. We use the spectrum of RX J1605.3+3249 as an illustration of the X-ray spectra of several other RQNSs with absorption features at $E \sim 0.3 - 0.4$ keV (see Table 1). In addition to the feature in the model spectrum at (redshifted) 0.4 keV, there are weaker absorption features at higher energies; these may be present in the spectrum of RX J1605.3+3249 or RX J1308.6+2127 (Haberl 2006). If all RQNSs have similar magnetic field strengths (e.g., $B \simeq \text{few} \times 10^{13}$ G, as suggested by timing analyses), we may expect RQNSs with higher temperatures to have more distinct absorption features at high energy (see, e.g., Figure 16). This appears to agree with the observed properties listed in Table 1. Further X-ray observations are needed to confirm the significance of multiple absorption lines.

On the other hand, it is puzzling as to why the spectrum of RX J1856.5–3754 can be fit by a featureless blackbody spectrum. Since RX J1856.5–3754 has a lower temperature than most of the other RQNSs, it is possible that molecular chains are formed on the surface (Medin & Lai 2006a,b), or RX J1856.5–3754 has the condensed surface (Turolla et al. 2004; van Adelsberg et al. 2005; Pérez-Azorín et al. 2005). Recent theoretical studies indicate that the condensed surfaces of magnetized NSs exhibit blackbody-like spectra in the X-ray band (Turolla et al. 2004; van Adelsberg et al. 2005; Pérez-Azorín et al. 2005). At the observed temperature of RX J1856.5–3754 ($T_{BB} \sim 7 \times 10^5$ K), it is estimated that a carbon atmosphere may become condensed when $B \gtrsim 3 \times 10^{13}$ G (Lai 2001; Medin & Lai 2006b). In this context, we expect that the other RQNS (RX J0420.0–5022) with a low temperature ($T_{BB} \sim 5 \times 10^5$ K) has a condensed surface; RX J0420–5022 should thus show a featureless blackbody-like spectrum³, unless it has a surface magnetic field lower than 10^{13} G. Indeed, the sharp temperature dependence of the molecular abundance was shown in the case of a helium atmosphere (Mori & Heyl 2007).

Optical flux excess from Rayleigh-Jeans tails of X-ray blackbody spectra is another common signature of RQNSs (Burwitz et al. 2003). Fully-ionized hydrogen atmosphere models overpredict the optical fluxes by 1–2 orders of magnitude (Pavlov et al. 1996; Pons et al. 2002). Unmagnetized heavy element atmosphere models can account for the optical excess (Pons et al. 2002), but they also exhibit numerous absorption features, which significantly deviate from the featureless X-ray spectra of RX J1856.5–3754 (Zavlin et al. 1996; Rajagopal & Romani

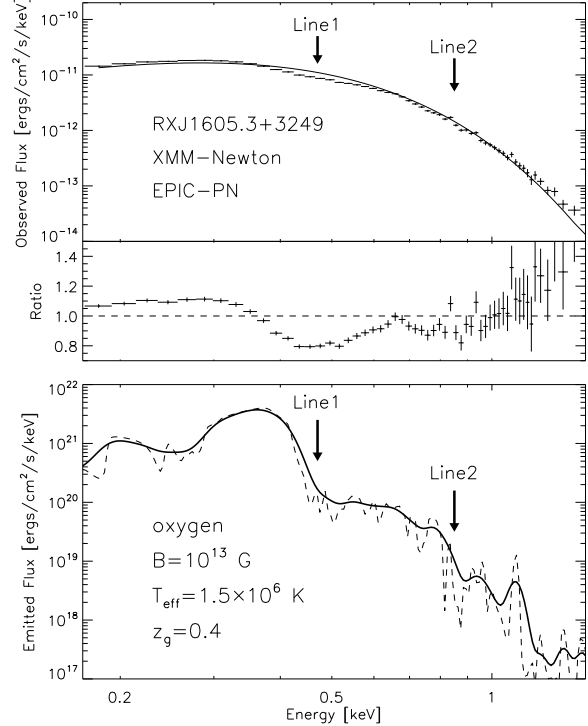


Figure 22. Unfolded *XMM-Newton* EPIC-PN spectrum of RXJ1605.3+3249 (top) and spectra of oxygen atmosphere with $B = 10^{13}$ G, $T_{\text{eff}} = 1.5 \times 10^6$ K and $z_g = 0.4$ (bottom). In the top panel, we overlaid a blackbody spectrum to illustrate the absorption features; we also show the ratio of the data and blackbody. In the bottom panel, the solid line is the model atmosphere spectrum convolved with the *XMM-Newton* EPIC-PN energy resolution, while the dashed line is the raw spectrum.

1996; Gänsicke et al. 2002). Therefore, it requires either a thin hydrogen atmosphere (Ho et al. 2007) or an anisotropic temperature distribution over the surface (Pons et al. 2002; Braje & Romani 2002; Pérez-Azorín et al. 2006) to produce both the featureless X-ray spectrum and the optical excess. Since magnetized mid-Z element atmospheres have SEDs close to blackbody, they may account for the optical excess. Unlike unmagnetized atmospheres, magnetic field variations can smear out absorption features in magnetized mid-Z atmosphere spectra and produce featureless X-ray spectra.

10 SUMMARY

We have constructed equation of state and opacity tables for mid-Z elements using the most up-to-date methods available and improving upon earlier calculations by including more physical effects. Using these tables, we built magnetic neutron star atmosphere models for carbon, oxygen, and neon. Mid-Z element atmosphere spectra show some dependence on magnetic field orientation (relative to the surface) and a weak dependence on surface gravity. There are many characteristics that distinguish these spectra from hydrogen atmosphere spectra, e.g., a multitude of lines, different line energy and strength dependences on the magnetic field, and possible hardening at high energies.

There are still several issues that need to be addressed in order to improve our models. These include accounting for molecules,

³ See caption (e) of table 1 for the current status of the putative line feature in the RX J0420.0–5022 spectrum.

the quantum electrodynamical effect of vacuum resonance, and non-LTE effects. Molecules and vacuum resonance may be important for atmosphere models with magnetic fields higher than those considered in this paper, i.e., $B \gg 10^{13}$ G (Ho & Mori 2007). We also plan to study atmosphere models with different elements, such as helium, silicon and iron, in order to cover a larger NS atmosphere parameter space. We will construct synthetic atmosphere model spectra by taking into account magnetic field and temperature distributions on the surface.

We presented qualitative comparisons between our model spectra and the observations of several isolated neutron stars. The results are promising; the model atmosphere spectra closely resemble the X-ray spectra of these objects. The similarities strongly motivate more detailed studies, including phase-resolved analysis, since line identification and a better temperature estimation can provide invaluable information on neutron stars.

ACKNOWLEDGEMENTS

KM thanks Dong Lai for the hospitality at Cornell University where this work was initiated. We are indebted to Dong Lai and Alexander Potekhin for their continuous support and many useful discussions. We also appreciate valuable comments from Marten van Kerkwijk, George Pavlov and Chris Thompson. We thank the anonymous referee for comments that helped to improve the paper. WH is grateful for the use of the computer facilities at the Kavli Institute for Particle Astrophysics and Cosmology. WH is partially supported by NASA through Hubble Fellowship grant HF-01161.01-A awarded by the Space Telescope Science Institute, which is operated by the Association of Universities for Research in Astronomy, Inc., for NASA, under contract NAS 5-26555.

REFERENCES

Alcock, C. & Illarionov, A. 1980, *ApJ*, 235, 534
 Babul, A. & Paczynski, B. 1987, *ApJ*, 323, 582
 Bezhastnov, V. G., Pavlov, G. G., & Ventura, J. 1998, *Phys. Rev. A*, 58, 180
 Bignami, G. F., Caraveo, P. A., Luca, A. D., & Mereghetti, S. 2003, *Nature*, 423, 725
 Braje, T. M. & Romani, R. W. 2002, *ApJ*, 580, 1043
 Bulik, T. & Pavlov, G. G. 1996, *ApJ*, 469, 373
 Burwitz, V., Haberl, F., Neuhäuser, R., Predehl, P., Trümper, J., & Zavlin, V. E. 2003, *A&A*, 399, 1109
 Chang, P., Arras, P., & Bildsten, L. 2004, *ApJL*, 616, L147
 Chang, P. & Bildsten, L. 2004, *ApJ*, 605, 830
 De Luca, A., Mereghetti, S., Caraveo, P. A., Moroni, M., Mignani, R. P., & Bignami, G. F. 2004, *A&A*, 418, 625
 de Vries, C. P., Vink, J., Méndez, M., & Verbunt, F. 2004, *A&A*, 415, L31
 Gänische, B. T., Braje, T. M., & Romani, R. W. 2002, *A&A*, 386, 1001
 Geppert, U., Küker, M., & Page, D. 2004, *A&A*, 426, 267
 —. 2006, *A&A*, 457, 937
 Ginzburg, V. L. 1970, The propagation of electromagnetic waves in plasmas (International Series of Monographs in Electromagnetic Waves, Oxford: Pergamon, 1970, 2nd rev. and enl. ed.)
 Greenstein, G. & Hartke, G. J. 1983, *ApJ*, 271, 283
 Griem, H. R. 1964, Plasma spectroscopy (New York: McGraw-Hill, 1964)
 Haberl, F. 2006, to appear in *Astrophysics and Space Science*, in the proceedings of "Isolated Neutron Stars: from the Interior to the Surface", edited by D. Page, R. Turolla and S. Zane, preprint (astro-ph/0609066)
 Haberl, F., Motch, C., Zavlin, V. E., Reinsch, K., Gänische, B. T., Cropper, M., Schweppe, A. D., Turolla, R., & Zane, S. 2004a, *A&A*, 424, 635
 Haberl, F., Schweppe, A. D., Hambaryan, V., Hasinger, G., & Motch, C. 2003, *A&A*, 403, L19
 Haberl, F., Turolla, R., de Vries, C. P., Zane, S., Vink, J., Méndez, M., & Verbunt, F. 2006, *A&A*, 451, L17
 Haberl, F., Zavlin, V. E., Trümper, J., & Burwitz, V. 2004b, *A&A*, 419, 1077
 Hailey, C. J. & Mori, K. 2002, *ApJL*, 578, L133
 Ho, W. C. G. & Mori, K. 2007, in preparation
 Ho, W. C. G., Kaplan, D. L., Chang, P., van Adelsberg, M., & Potekhin, A. Y. 2007, *MNRAS*, 375, 821
 Ho, W. C. G. & Lai, D. 2001, *MNRAS*, 327, 1081
 —. 2003, *MNRAS*, 338, 233
 —. 2004, *ApJ*, 607, 420
 Ho, W. C. G., Lai, D., Potekhin, A. Y., & Chabrier, G. 2003, *ApJ*, 599, 1293
 Ichimaru, S., Iyetomi, H., & Tanaka, S. 1987, *Phys. Rep.*, 149, 91
 Kaplan, D. L. & van Kerkwijk, M. H. 2005a, *ApJL*, 628, L45
 —. 2005b, *ApJL*, 635, L65
 Kaplan, D. L., van Kerkwijk, M. H., & Anderson, J. 2002, *ApJ*, 571, 447
 Khersonskii, V. K. 1987, *AZh*, 64, 433
 Lai, D. 2001, *Rev. Mod. Phys.*, 73, 629
 Lai, D. & Salpeter, E. E. 1997, *ApJ*, 491, 270
 Lattimer, J. M. & Prakash, M. 2001, *ApJ*, 550, 426
 Lloyd, D. A. 2003, *MNRAS*, submitted (astro-ph/0303561)
 London, R. A., Taam, R. E., & Howard, W. M. 1986, *ApJ*, 306, 170
 Madej, J., Joss, P. C., & Różańska, A. 2004, *ApJ*, 602, 904
 Medin, Z. & Lai, D. 2006a, *Phys. Rev. A*, 74, 062507
 —. 2006b, *Phys. Rev. A*, 74, 062508
 Mereghetti, S., De Luca, A., Caraveo, P. A., Becker, W., Mignani, R., & Bignami, G. F. 2002, *ApJ*, 581, 1280
 Mészáros, P. 1992, High-energy radiation from magnetized neutron stars (Theoretical Astrophysics, Chicago: University of Chicago Press, —c1992)
 Mihalas, D. 1978, Stellar atmospheres /2nd edition/ (San Francisco, W. H. Freeman and Co., 1978. 650 p.)
 Miller, M. C. 1992, *MNRAS*, 255, 129
 Mori, K., Chonko, J. C., & Hailey, C. J. 2005, *ApJ*, 631, 1082
 Mori, K. & Hailey, C. J. 2002, *ApJ*, 564, 914
 —. 2006, *ApJ*, 648, 1139
 Mori, K. & Heyl, J. 2007, *MNRAS*, in press, preprint (astro-ph/0610253)
 Özel, F. 2001, *ApJ*, 563, 276
 Paerels, F. 1997, *ApJL*, 476, L47
 Page, D., Lattimer, J. M., Prakash, M., & Steiner, A. W. 2004, *ApJS*, 155, 623
 Pavlov, G. G. & Meszaros, P. 1993, *ApJ*, 416, 752
 Pavlov, G. G. & Potekhin, A. Y. 1995, *ApJ*, 450, 883
 Pavlov, G. G., Shibanov, Yu. A., Ventura, J., & Zavlin, V. E. 1994, *A&A*, 289, 837
 Pavlov, G. G., Shibanov, Yu. A., Zavlin, V. E., & Meyer, R. D. 1995, in The Lives of the Neutron Stars. Proceedings of the NATO Advanced Study Institute on the Lives of the Neutron

Stars, Publisher, Kluwer Academic, Dordrecht, The Netherlands, Boston, Massachusetts, 1995. p.71

Pavlov, G. G., Zavlin, V. E., Truemper, J., & Neuhaeuser, R. 1996, *ApJL*, 472, L33

Pérez-Azorín, J. F., Miralles, J. A., & Pons, J. A. 2005, *A&A*, 433, 275

—. 2006, *A&A*, 451, 1009

Pons, J. A., Walter, F. M., Lattimer, J. M., Prakash, M., Neuhaeuser, R., & An, P. 2002, *ApJ*, 564, 981

Potekhin, A. Y. 1994, *J. Phys. B*, 27, 1073

Potekhin, A. Y. & Chabrier, G. 2003, *ApJ*, 585, 955

—. 2004, *ApJ*, 600, 317

Potekhin, A. Y., Chabrier, G., & Gilles, D. 2002, *Phys. Rev. E*, 65, 36412

Potekhin, A. Y., Chabrier, G., & Shibanov, Y. A. 1999, *Phys. Rev. E*, 60, 2193

Potekhin, A. Y., Lai, D., Chabrier, G., & Ho, W. C. G. 2004, *ApJ*, 612, 1034

Potekhin, A. Y., Massacrier, G., & Chabrier, G. 2005, *Phys. Rev. E*, 72, 046402

Potekhin, A. Y. & Pavlov, G. G. 1997, *ApJ*, 483, 414

Rajagopal, M. & Romani, R. W. 1996, *ApJ*, 461, 327

Rajagopal, M., Romani, R. W., & Miller, M. C. 1997, *ApJ*, 479, 347

Romani, R. W. 1987, *ApJ*, 313, 718

Salzmann, D. 1998, *Atomic Physics in Hot Plasmas* (New York: Oxford University Press, 1998)

Sanwal, D., Pavlov, G. G., Zavlin, V. E., & Teter, M. A. 2002, *ApJL*, 574, L61

Schwone, A. D., Hambaryan, V., Haberl, F., & Motch, C. 2005, *A&A*, 441, 597

Shibanov, I. A., Zavlin, V. E., Pavlov, G. G., & Ventura, J. 1992, *A&A*, 266, 313

Turbiner, A. V. & López Vieyra, J. C. 2004, *Modern Physics Letters A*, 19, 1919

Turolla, R., Zane, S., & Drake, J. J. 2004, *ApJ*, 603, 265

van Adelsberg, M. & Lai, D. 2006, *MNRAS*, 373, 1495

van Adelsberg, M., Lai, D., Potekhin, A. Y., & Arras, P. 2005, *ApJ*, 628, 902

van Kerkwijk, M. H. & Kaplan, D. L. 2006, to appear in *Astrophysics and Space Science*, in the proceedings of "Isolated Neutron Stars: from the Interior to the Surface", edited by D. Page, R. Turolla and S. Zane, preprint (astro-ph/0607320)

van Kerkwijk, M. H., Kaplan, D. L., Durant, M., Kulkarni, S. R., & Paerels, F. 2004, *ApJ*, 608, 432

van Kerkwijk, M. H. & Kulkarni, S. R. 2001, *A&A*, 380, 221

Vink, J., de Vries, C. P., Méndez, M., & Verbunt, F. 2004, *ApJL*, 609, L75

Walter, F. M. & Lattimer, J. 2002, *ApJL*, 576, L145

Woods, P. M., Zavlin, V. E., & Pavlov, G. G. 2006, to appear in *Astrophysics and Space Science*, in the proceedings of "Isolated Neutron Stars: from the Interior to the Surface", edited by D. Page, R. Turolla and S. Zane, preprint (astro-ph/0608483)

Yakovlev, D.G. & Pethick, C.J. 2004, *ARA&A*, 42, 169

Zane, S., Cropper, M., Turolla, R., Zampieri, L., Chieregato, M., Drake, J. J., & Treves, A. 2005, *ApJ*, 627, 397

Zane, S. & Turolla, R. 2006, *MNRAS*, 366, 727

Zane, S., Turolla, R., & Treves, A. 2000, *ApJ*, 537, 387

Zane, S., Turolla, R., Stella, L., & Treves, A. 2001, *ApJ*, 560, 384

Zavlin, V. E., Shibanov, Y. A. & Pavlov, G. G. 1995, *A&A*, 297, 441

Zavlin, V. E., Pavlov, G. G., & Shibanov, Y. A. 1996, *A&A*, 315,